

# A novel CVD Method for Rapid Fabrication of Superhydrophobic Surface on Aluminum Alloy Coated Nanostructured Cerium-Oxide and Its Corrosion Resistance

*Kai Zhang, Junsheng Wu<sup>\*</sup>, Pingping Chu, Yuanzheng Ge, Ruitao Zhao, Xiaogang Li*

Institute of Advanced Materials and Technology, University of Science and Technology Beijing, No.30 Xueyuan Rd., Haidian Distr., Beijing, 100083, P.R. China

\*E-mail: [wujis@ustb.edu.cn](mailto:wujis@ustb.edu.cn)

*Received: 24 April 2015 / Accepted: 29 May 2015 / Published: 24 June 2015*

---

An facile CVD method of fabricating a superhydrophobic coating on aluminum alloy was reported in this paper. The rough surface structure could be easily obtained by hydrothermal deposition of cerium oxide. The rough surface could be changed from superhydrophilic to superhydrophobic by modification with 1H,1H,2H,2H-perfluorooctyltriethoxysilane. The as-prepared coatings were characterized by scanning electron microscopy (SEM), contact angle measurement, and Fourier transform infrared spectroscopy. The influence of boiling water treatment on the micro/nano-structure of cerium-oxide film was elucidated by SEM. The anticorrosion property of the superhydrophobic cerium-oxide film on aluminum alloy in 3.5 wt. % NaCl aqueous solution was investigated using linear polarization, open-circuit potential curve, and electrochemical impedance spectroscopy analyses. The effect of transformation between the Wenzel and Cassie–Baxter states on corrosion resistance was studied. Results showed that superhydrophobic film in Cassie–Baxter state had a better protection. Electrochemical results revealed that the superhydrophobic cerium-oxide film significantly improved the corrosion resistance of aluminum alloy, and the stable air cushion formed on the superhydrophobic surface was essential to the improvement of the anticorrosion property.

---

**Keywords:** aluminum alloy; superhydrophobic; cerium oxide; corrosion resistance; 1H,1H,2H,2H-perfluorooctyltriethoxysilane

## 1. INTRODUCTION

Researchers have studied various kinds of creatures' surface and found that hydrophobicity is associated with the microstructure of such surface[1-3]. Barthlott found that hydrophobicity is closely related to the surface topography of these plants and suggested that superhydrophobicity is due to

superficial microroughness[4]. Jiang successfully constructed an artificial superhydrophobic surface by mimicking the superhydrophobic surface structure in nature[5, 6]. Apart from micro/nano-surface roughness, the lower interface energy was also indispensable to fabricate superhydrophobic surface.

The special properties of superhydrophobic surfaces are gaining considerable attention, including their self-cleaning, non-wetting, antifouling, and anticorrosion abilities[7-10]. Superhydrophobic surfaces could isolate metals from corrosion electrolyte and protect metals from corrosion. Zhang proved that the corrosion resistance of superhydrophobic films was highly associated with the formation of air cushion on this surface[11, 12]. Li showed that superhydrophobic films on magnesium alloy had excellent corrosion resistance[13]. Given the excellent corrosion resistance property of superhydrophobic films, the anticorrosion mechanism has been studied. Liu found that air trapped in superhydrophobic surfaces could generate a capillary effect that prevents  $\text{Cl}^-$  ions from reaching the substrate, thereby significantly improving the metal's anticorrosion property[14]. Ishizaki, Torchinsky, and Wang demonstrated that the anticorrosion mechanism of superhydrophobic films was a synergy of capillary and air cushion effects[15-17].

Meanwhile, Zhang found that the corrosion resistance of superhydrophobic films varied with the contact models, namely, the Wenzel and Cassie–Baxter models[18-20]. In the Wenzel model, the liquid may completely penetrate the rough grooves[21]. In the Cassie–Baxter model, the liquid is in contact with the solid and trapped air instead of penetrating the grooves. However, studies about the effect of the contact model on the corrosion resistance of superhydrophobic film and about the effect of the transformation between the two contact models on corrosion are few.

Cerium compounds have been used to protect aluminum alloys against corrosion for the past three decades[22-24]. William G. Fahrenholtz studied the corrosion protection of cerium-based conversion coatings formed on aluminum alloy 7075-T6 substrates, which could inhibit corrosion for 336 h in neutral salt fog testing as per ASTM B117[22]. Given the excellent anticorrosion property of superhydrophobic cerium-oxide film, it is worth fabricating as an anticorrosion layer. Ishizaki and Jin had fabricated nanostructured cerium-oxide film on magnesium and aluminum alloy and made this surface get superhydrophobicity in liquid phase method[25-27]. However, there were no further study of the formation mechanism of the micro/nano structure and the relationship between superhydrophobic film's corrosion resistance and contact models.

In this paper, we constructed a unique rough nano-petal structure on aluminum, which was simply treated by cerium nitrate aqueous solution. An excellent superhydrophobic surface was obtained rapidly by a novel CVD method. The anticorrosion property of the superhydrophobic film was systematically studied in two different contact models.

## 2. EXPERIMENTAL DETAILS

### 2.1 Materials

The following materials were used in the study: aluminum alloy 2024 (heat treatment T3, composition: Cu 3.8–4.9%, Mg 1.3–1.8%, Mn 0.30–0.9 %, Si 0.1–0.25%, Zn $\leq$ 0.30%, Al% Bal.), cerium (III) nitrate hexahydrate ( $\text{Ce}(\text{NO}_3)_3 \cdot 6\text{H}_2\text{O}$ ; Tianjin Guangfu Fine Chemical Research Institute),

hexamethylenetetramine ( $C_6H_{12}N_4$ ; Beijing Chemical Works), ethyl alcohol absolute ( $C_2H_5OH$ ; Beijing Chemical Works), 1H,1H,2H,2H-perfluorooctyltriethoxysilane (PFOTES; Zhejiang Research Institute of Chemical Industry, Ltd., 97%), acetone ( $CH_3COCH_3$ ; Beijing Chemical Works), ammonium hydroxide ( $NH_3 \cdot H_2O$ ; Sinopharm Chemical Reagent Co., Ltd; 25–28). The deionized water used was Milli-Q water (Milli-Q, USA). All reagents were analytical grade and used as received without further purification. The dimensions of the specimens were 50 mm  $\times$  25 mm  $\times$  4 mm and 10 mm  $\times$  10 mm  $\times$  4 mm.

## 2.2 Experimental procedures

### 2.2.1 Fabrication of cerium-oxide film

All aluminum substrates were sequentially polished with #240, #400, #800, #1000, #1500, #2000, and #3000 sandpapers and then ultrasonically cleaned in acetone, absolute ethanol, and deionized water for 10 min, respectively. After cleaning, the substrates were dried with  $N_2$ . Part of the sample was treated in boiling deionized water for 2 min and dried with  $N_2$ .

2.174 g of  $Ce(NO_3)_3 \cdot 6H_2O$  and 10.514 g of  $C_6H_{12}N_4$  were dissolved in 50 ml deionized water, respectively [27]. The two solutions were heated to 70 °C in thermostat water bath for 30 min in advance. After the two solutions were mixed together, the only ultrasonically cleaned samples (USs) and boiling water-treated samples (BSs) were immersed in the mixed solution immediately. The samples were heated to 70 °C for 1 h together with the mixed solution to undergo an in situ growth process of cerium oxide. Then, the samples were rinsed with deionized water and blow dried with  $N_2$ .

### 2.2.2 Fabrication of superhydrophobic surface

Samples coated with cerium-oxide film were modified with a novel CVD method and a conventional liquid-phase method. For CVD method, samples together with two beakers containing 0.2 ml PFOTES and 0.1 ml distilled water were installed in a temperature controlled chamber with a volume of 250 ml. After the chamber was sealed, the reaction was processed 1 h, 6 h, 12 h and 24 h under 120 °C. The deionized water was used as a catalyst to promote the hydrolysis of PFOTES molecules. There was no any further treatment.

For the conventional liquid-phase method, samples were immersed in 200 ml of an absolute ethanol solution containing 0.6 mL of PFOTES and 0.1 mL of deionized water, and the reaction was processed 1 h, 6 h, 12 h, 24 h, 72 h, 120 h, and 168 h under 50 °C. Subsequently, the samples were dried at room temperature for at least 2 h and annealed at 120 °C for 2 h with a ramping rate of 1 °C per minute to remove the residual solvent.

## 2.3 Characterization

Morphology analysis was performed using a scanning electron microscopy (SEM, Quanta 250). Static water contact angle (CA) of the surfaces were estimated with an OCA 20 using a water drop

volume of 4  $\mu\text{L}$ . The average CA was determined by measuring the same substrate at five different positions. Fourier transform infrared (FTIR) spectra were recorded with a Magna-IR 750 FTIR spectrophotometer. The electrochemical properties of the as-obtained substrate surface were determined in 3.5 wt.% NaCl aqueous solution using an electrochemical workstation (Autolab, PGSTAT302N) equipped with a standard three-electrode system (saturated calomel electrode (SCE), platinum as the counter electrode, and sample with 3.14  $\text{cm}^2$  exposed to the electrolytic solution as the working electrode). Linear polarization curves were obtained at a scanning rate of  $0.3 \text{ mV}\cdot\text{s}^{-1}$  from -200 mV to 800 mV (vs. open circuit potential,  $E_{\text{ocp}}$ ). Corrosion current densities ( $i_{\text{corr}}$ ) and corrosion potential ( $E_{\text{corr}}$  vs. SCE) were obtained by extrapolating the linear portions of the anodic and cathodic branched to their intersection using a previously described procedure[24]. Electrochemical impedance spectroscopy (EIS) measurements were conducted within the frequency range of 100 KHz to 0.01 Hz at  $E_{\text{ocp}}$  with an amplitude of perturbation voltage of 10 mV. All measurements were made at room temperature.

### 3. RESULTS AND DISCUSSION

#### 3.1 Morphology

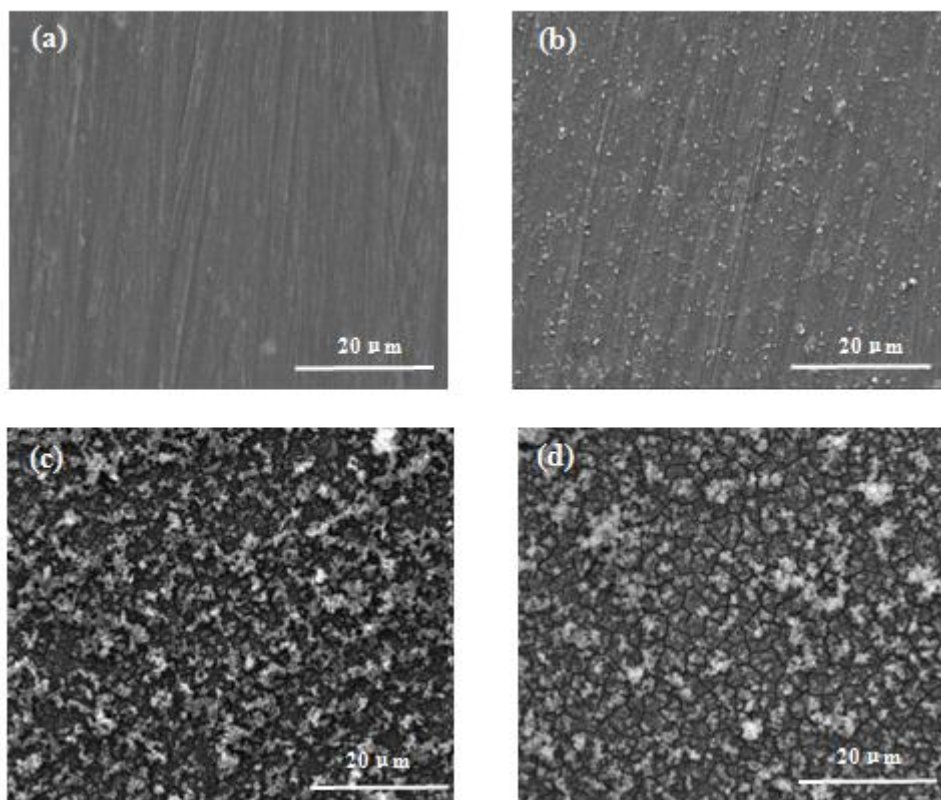


**Figure 1.** SEM image of cerium-oxide films on USs after hydrothermal treatment in cerium nitrate aqueous solution for different times: (a) 0 min, (b) 1 min, (c) 10 min, and (d) 60 min

Fig. 1 shows the SEM image of cerium-oxide films on USs after hydrothermal process in cerium nitrate aqueous solution at 70 °C for different times. Fig. 1 (a) and (c) show that cerium-oxide particles were physically absorbed non-selectively on the USs. The initial cerium-oxide particle formed on the USs could be low-energy points and then became an active patch. Other cerium-oxide particles in the solution preferentially grew around those active patches. With prolonged hydrothermal time, a rough surface structure was formed on the USs. However, more cracks were observed with increased cerium-oxide film growth (Fig. 1(c) and 1(d)). This finding was due to the contraction of cerium-oxide film when the samples were blow dried after the hydrothermal process, thereby generating stress and leading to crack formation. As the film became thicker, stress was enhanced and more cracks formed. Given the existence of these cracks, the material cannot be used as an anticorrosion film.

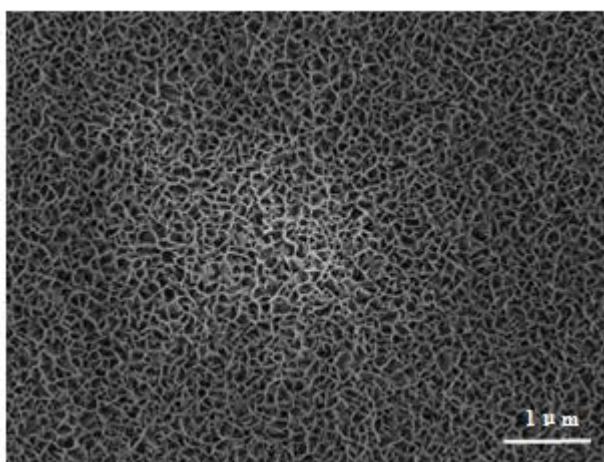


**Figure 2.** SEM images of USs after boiling water treatment for 2 min

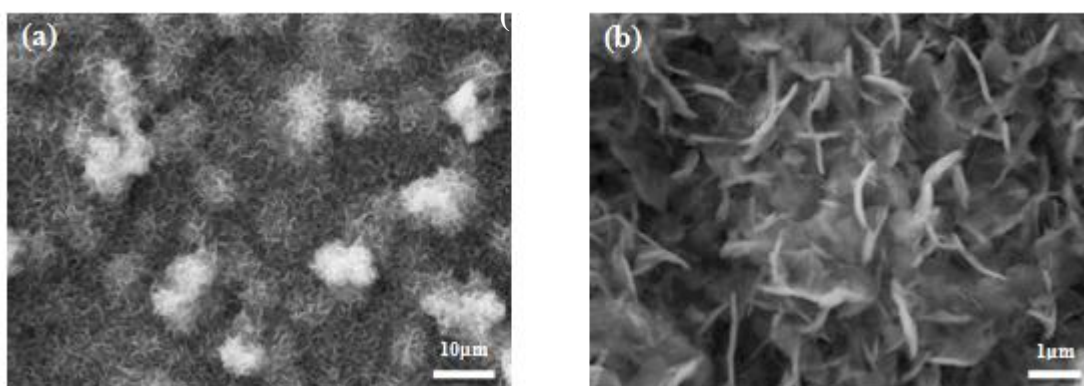


**Figure 3.** (a) SEM image of BSs after hydrothermal treatment in cerium nitrate aqueous solution for 1 h; (b) Enlarged cerium-oxide film SEM image

To construct a uniform cerium-oxide film with micro/nano-rough structure, aluminum substrates were pretreated with boiling water to fabricate an alumina surface with nano-rough

structure. Under the structure-direction control of the alumina structure, cerium-oxide film with flower-like structure was fabricated on aluminum by a hydrothermal process. USs were treated with boiling water for 2 min (Fig. 2). Fig. 3 shows the morphology of BSs after hydrothermal treatment in cerium nitrate solution for 1h. A flower-like structure of cerium-oxide was formed, and no apparent cracks were observed. To investigate the formation mechanism of the flower-like structure, the relationship between the structure and hydrothermal time was studied by SEM (Fig. 4).

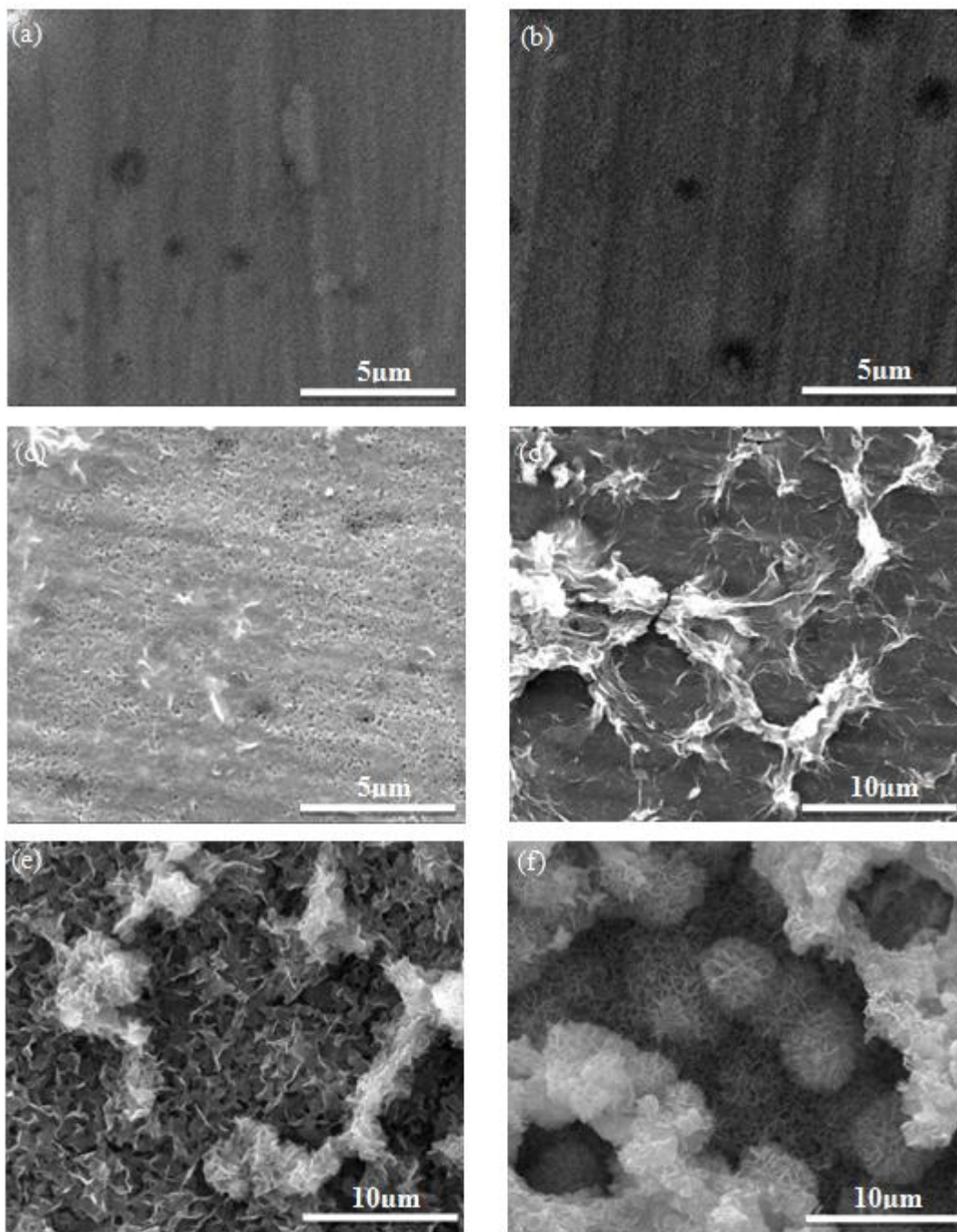
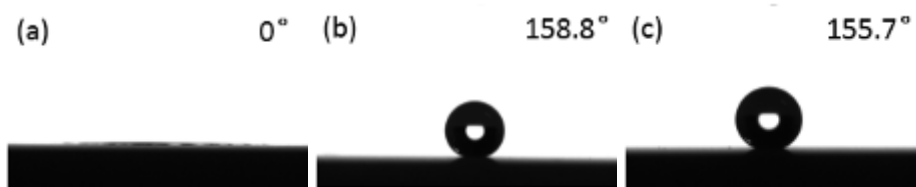


**Figure 4.** Typical SEM image of cerium-oxide films under the molar ratio of  $\text{Ce}(\text{NO}_3)_3 \cdot 6\text{H}_2\text{O}$  to  $\text{C}_6\text{H}_{12}\text{N}_4\text{O}_{15}$ :1 on WB surface for different time: (a) 0 min, (b) 5 min, (c) 10 min, (d) 20 min, (e) 30 min and (f) 60min

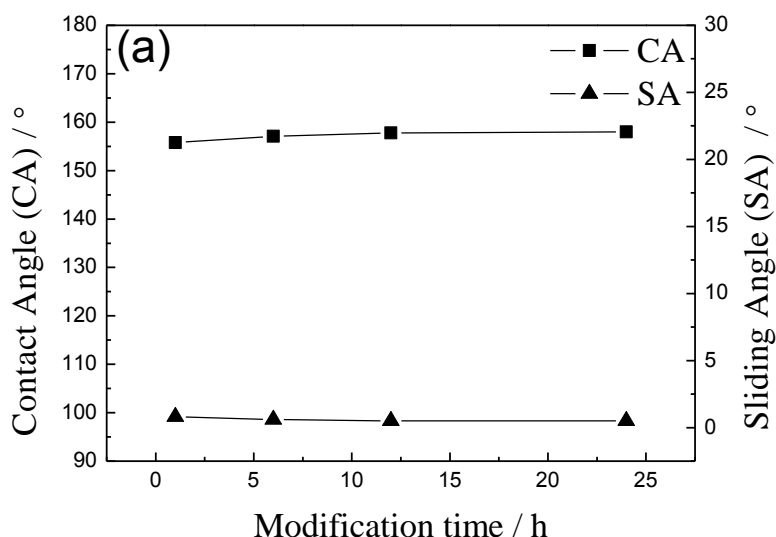
Fig. 4 (a–f) show no significant change before 5 min of hydrothermal treatment. In this stage, cerium-oxide preferentially nucleated on the roof of AlO(OH) because of its low energy. When the hydrothermal time was extended to 10 min, a cerium-oxide film with some pores covered the BSs. The preferentially selective growth on the roof was attributed to these pores. With further prolonged time to 20 min, the cerium-oxide film completely covered the BSs, but some protuberances were observed. After treatment for over 30 min, these protuberances grew into nanosheets and finally aggregated together to form a flower-like structure. Therefore, the structure formed on the BSs after boiling water treatment played a vital role in structure directing and contributed to the selective nucleus and in situ growth of cerium oxide. A hierarchical micro-nanostructure was formed on aluminum surface. The surface of the cerium-oxide film was textured with 3–8 μm size flower-like structures decorated with 50–300 nm-sized sheets (Fig. 3). Furthermore, given the non-existence of cracks, the material can be used as an anticorrosion film.

### 3.2 Superhydrophobicity

#### 3.2.1 CVD method



**Figure 5.** WCA images of cerium-oxide film: (a) before modification, (b) after modification with PFOTES by CVD method for 1 h, and (c) modified by PFOTES ethanol solution for 1 h



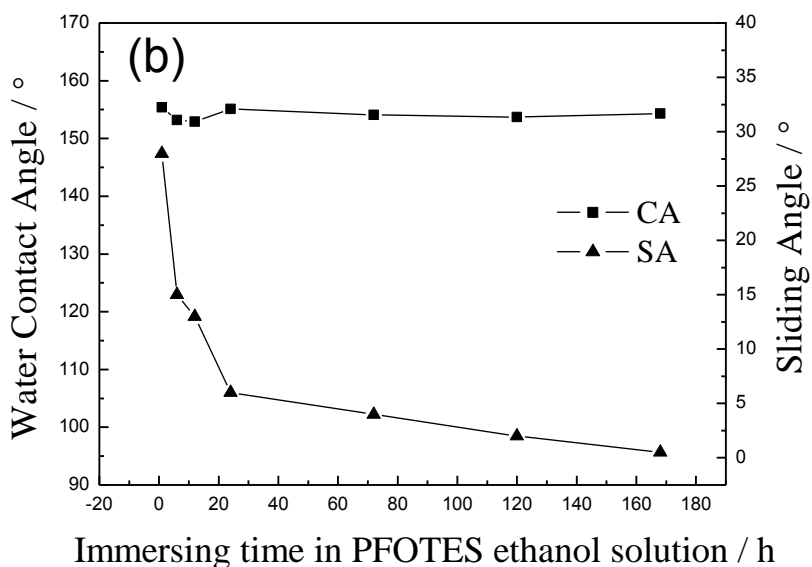


**Figure 6.** Relationship between the CA and SA of the as-prepared superhydrophobic film: (a) modified by CVD method; (b) modified in PFOTES ethanol solution

Before modification of the as-prepared cerium-oxide film, the CA was about 0° (Fig. 5(a)). By CVD method, the cerium-oxide surface gained superhydrophobicity after the reaction only processed 1 h in 120 °C as shown in Fig. 5(b). Fig. 6(a) showed small changes in WCA and sliding angle (SA), with SA being < 1° with prolonged modification time. Moreover, water droplets on these samples hardly stayed on the surface and rapidly rolled off when slightly disturbed.

### 3.2.2 Liquid-phase method

As presented in Fig. 6(b), CA reached 155.7° and showed superhydrophobicity after 1 h of immersion in PFOTES ethanol solution. Fig. 5(c) showed the behaviors of water droplets on the cerium-oxide film modified by PFOTES ethanol solution for 1 h.

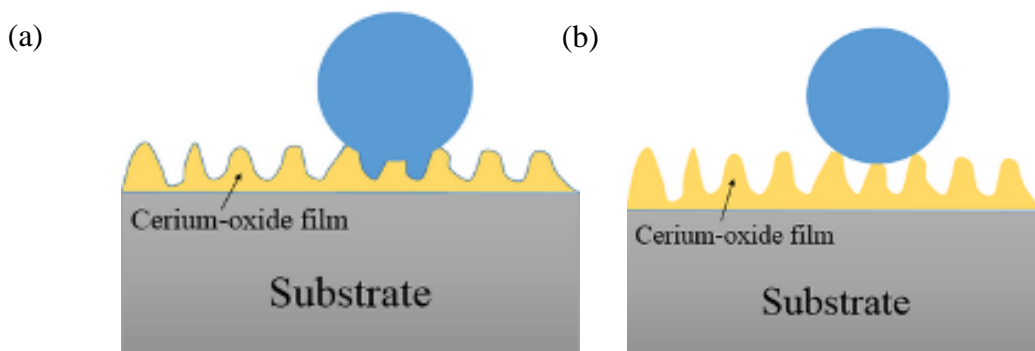


**Figure 7.** Interface model of the (a) Wenzel and (b) Cassie–Baxter states

The CA changed very little with prolonged immersing time (Fig. 6(b)). However, SA decreased gradually with further prolonged immersing time. After immersing in PFOTES ethanol solution for 168 h, the SA was  $<1^\circ$ . As immersing time increased, more PFOTES covered the cerium-oxide film and SA decreased. This change in SA indicated the transformation of contact state. After immersion for 1 h, the contact state could be defined as Wenzel state (Fig. 7(a)); after immersing for 168 h, the contact state transformed to Cassie–Baxter state (Fig. 7(b)). The trapped air prevented water from penetrating into the pores. This phenomenon was in favor of the rolling resistance reduction of electrolyte. Compared with the result of CVD method, liquid-phase method spent more time and cost than CVD method to achieve the desired hydrophobicity. Therefore, CVD was superior to liquid-phase method because of the higher efficiency of reaction between PFOTES and  $-OH$  on the sample.

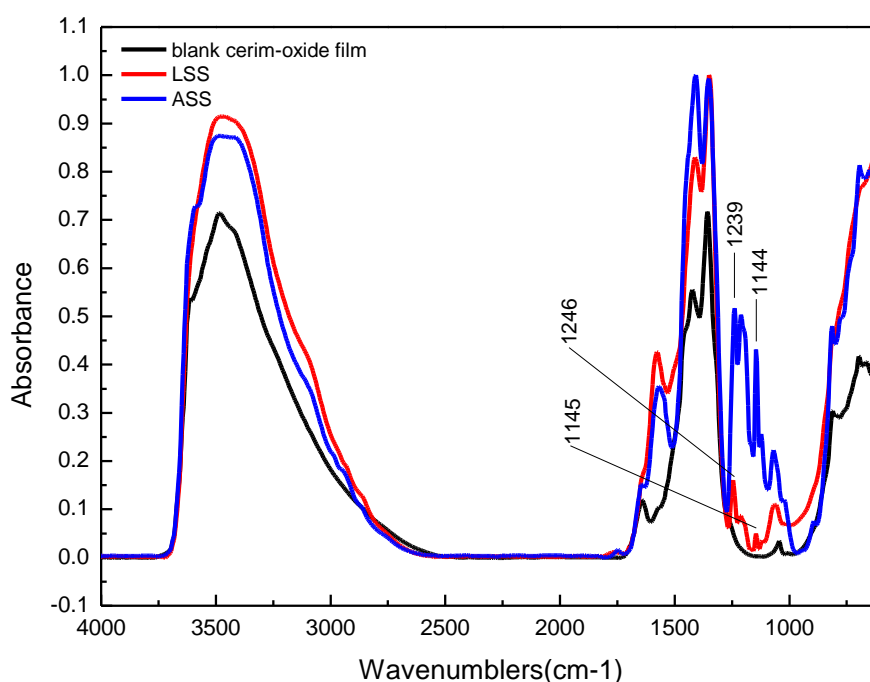


**Figure 8.** Fourier transform infrared spectra of blank cerium-oxide film, LSS, and ASS

Fig. 8 presents the FTIR spectra of blank cerium-oxide film, superhydrophobic samples modified by liquid-phase method (LSS) and modified by CVD method (ASS). The absorption bands that appeared at  $1144\text{ cm}^{-1}$ ,  $1145\text{ cm}^{-1}$ ,  $1239\text{ cm}^{-1}$  and  $1246\text{ cm}^{-1}$  were contributed to the vibrations of  $\text{CF}_2$  and  $\text{CF}_3$  group in PFOTES [28,29]. The absorption peaks at  $700\text{--}800\text{ cm}^{-1}$  were due to the vibration of Si-O group in the silanes. The FTIR result verified the successful formation of the low free energy groups on the surface of the cerium-oxide film. Furthermore, the absorbance intensity of  $\text{CF}_2$  and  $\text{CF}_3$  group on ASS was higher than that of  $\text{CF}_2$  and  $\text{CF}_3$  group on LSS. Thus, more PFOTES covered on the cerium-oxide film in CVD process. This also proved that CVD method used for

PFOTES modification shows faster deposition speed and higher reaction efficiency than the liquid-phase immersion method.

### 3.3 Anticorrosion

#### 3.3.1 Linear polarization

According to common knowledge, SA is associated with the contact state. To study the effect of contact state on anticorrosion property, samples coated with cerium-oxide film were modified in PFOTES ethanol solution for different time, and superhydrophobicity was attained with different contact state (Fig. 6(b)). Linear polarization (LP) was used to evaluate the corrosion behavior of the films with different liquid-solid contact state in 3.5 wt. % NaCl aqueous solution.

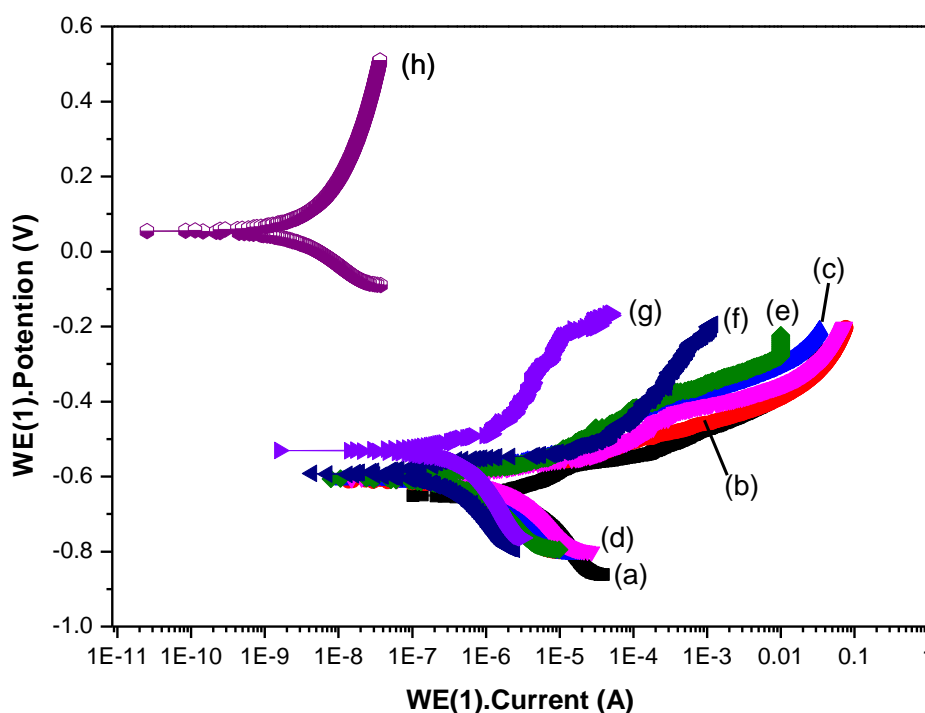


**Figure 9.** Linear polarization curves of (a) untreated aluminum substrate; (b) coated with cerium-oxide film; and superhydrophobic surfaces formed on aluminum coated cerium-oxide film after immersion in 0.6% PFOTES ethanol solution for (c) 1 h, (d) 12 h, (e) 24 h, (f) 72 h and (g) 168 h; (h) modified by CVD for 24 h

Fig. 9 shows that the corrosion potential ( $E_{\text{corr}}$  vs SCE) of the superhydrophobic sample immersed in PFOTES ethanol solution for 168 h was  $-0.530$  V (Table 1), considerably shifting to the positive direction compared with the cerium-oxide film coated aluminum ( $-0.652$  V, Table 1). The

$E_{\text{corr}}$  values of the superhydrophobic surfaces formed on aluminum coated cerium-oxide film after immersion in 0.6% PFOTES ethanol solution for 1 h, 12 h, 24 h, and 72 h were -0.612 V, -0.605 V, -0.605 V, and -0.593 V (Table 1), respectively.  $E_{\text{corr}}$  was found to shift to the positive direction with increased immersing time in PFOTES ethanol solution. Moreover, the linear polarization curve measurements indicated that the anticorrosion resistance was obviously improved by the superhydrophobic treatment. The corrosion current density,  $I_{\text{corr}}$ , of the superhydrophobic surface ( $0.002\mu\text{A}/\text{cm}^2$ ) modified by CVD method decreased by more than 3 orders of magnitude as compared to that of the untreated sample ( $8.69\mu\text{A}/\text{cm}^2$ ). According to the results of the superhydrophobically treated magnesium alloy by liquid-phase immersion method, the corrosion current density decreased by more than 1 order of magnitude as compared to that of substrate[27].

**Table 1.** Linear Polarization parameters of substrate, unmodified cerium oxide film (CO), cerium oxide film modified in PFOTES ethanol solution for 1 h, 12 h, 24 h, 72 h and 168 h, and cerium oxide film modified by CVD method for 24 h

	$E_{\text{corr}}$ (V)	$I_{\text{corr}}$ ( $\mu\text{A}/\text{cm}^2$ )	$\beta_c$ (mV)	$\beta_a$ (mV)
substrate	-0.658	8.69	1219.4	39.1
CO	-0.652	3.647	236.5	69.2
1 h	-0.612	0.79	192.7	44.1
12 h	-0.605	0.78	109.1	43.3
24 h	-0.605	0.51	176.5	58.7
72 h	-0.593	0.30	241	27.9
168 h	-0.530	0.07	41.3	32.4
CVD 24h	0.055	0.002	149.2	204.3

The positive shift of the  $E_{\text{corr}}$  could attribute to the transfer of contact state on the superhydrophobic surface. In prolonging the immersing time, the contact state transferred from Wenzel state to Cassie–Baxter state, and the SA decreased (Fig. 6(b)). As SA decreased, more air was trapped in the hierarchical micro-nanostructure. As the SA was lower than  $1^\circ$ , a complete air layer was formed. Due to the air layer, electrolyte could not penetrate into the film. The air layer preserved the aluminum from corrosion. Therefore, the trapped air played an important role in inhibiting the corrosion of aluminum, and the superhydrophobic cerium-oxide film with Cassie–Baxter state had superior corrosion resistance performance.

Furthermore, The  $E_{\text{corr}}$  of the superhydrophobic sample modified by CVD method for 24 h was more positive than superhydrophobic samples modified in PFOTES ethanol solution for 168 h. The  $E_{\text{corr}}$  of the superhydrophobic sample modified by CVD method was 0.055 V (Table 1). It showed more excellent anticorrosion property.

3.3.2 Open Circuit Potential

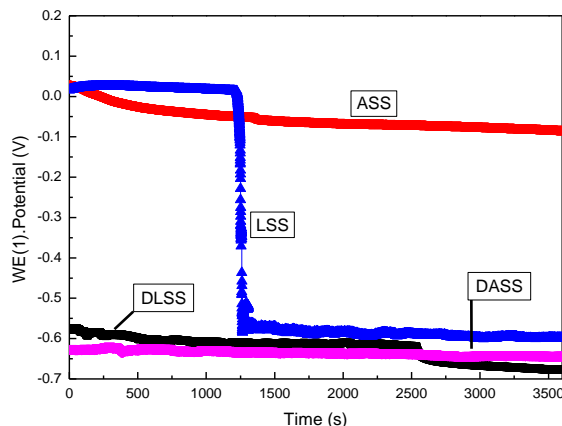
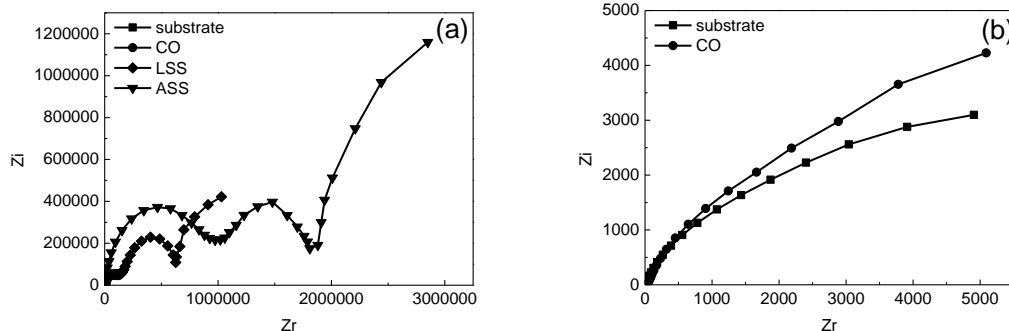
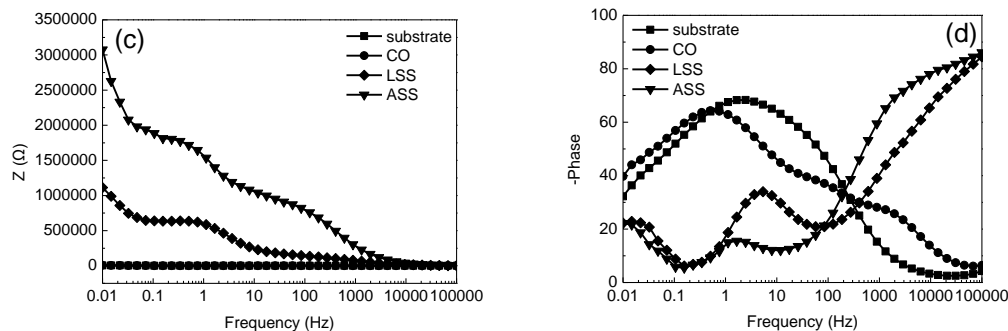


Figure 10. Eoc – t curves of LSS, ASS, DLSS and DASS in 3.5% NaCl solution

To investigate the contribution of the trapped air, a deaeration process was adopted [5, 9]. The result of  $E_{oc}$ -t verified the role of the trapped air (Fig. 10). As the immersing time increased in 3.5 wt. % NaCl solution, the  $E_{oc}$  of superhydrophobic samples modified by CVD method (ASS) changed little and kept at the range of 0.03 V to -0.08 V. Nevertheless, superhydrophobic samples modified by liquid-phase method significantly changed at 1200 s, and finally kept around -0.56 V, indicating the failure of the superhydrophobic film. Note that the  $E_{oc}$  of the deaerated superhydrophobic films (DLSS and DASS) was at the range of -0.57 V to -0.68 V, which were more negative than ASS. Comparing the  $E_{oc}$ -t curves, it indicated that air layer trapped on ASS was more stable than that of LSS, due to more PFOTES covering on cerium-oxide film in CVD process. Furthermore, it demonstrated that the trapped air contributed to the anticorrosion property of the superhydrophobic film, and the trapped air in ASS was more stable than that in LSS. The deaeration weakened the anti-corrosion performance of the superhydrophobic film.

3.3.3 EIS

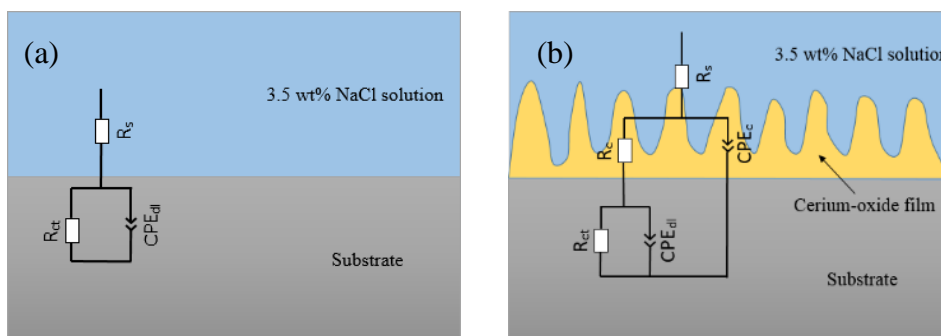




**Figure 11.** (a) Nyquist plot of the substrate, substrate coating cerium-oxide film, LSS and ASS in 3.5 wt.% NaCl aqueous solution; (b) Enlarged impedance spectra; (c) Bode plots of  $|Z|$  vs. frequency and (d) Bode plots of phase angle vs. frequency

The typical EIS plots of the substrate, cerium-oxide film coating on aluminum (CO), LSS and ASS were shown in Fig. 11. The enlarged impedance spectra were shown in Fig. 11(b). Three time constants could be observed for LSS and ASS (Fig. 11(a)); however, one and two time constants were observed for substrate and CO (Fig. 11(b)), respectively. The high frequency capacitance loop was related to the trapped air on superhydrophobic film. Attributing it to the more stable air layer formed on the ASS, the radius of the high frequency capacitance loop was bigger than that of LSS. Furthermore, the phase angle of LSS and ASS reached  $87^\circ$ , and the phase angle of ASS in high frequency region was higher than LSS. This finding can be attributed to the trapped air layer. Due to more PFOTES covered on the cerium-oxide film in CVD process, a more stable and intact air layer could form and little conductive pass ways could be formed.

The Bode plots were shown in Fig. 11(c) and (d). In general, the impedance behavior in the low frequency region reflected the charge transfer resistance  $R_{ct}$  and double layer capacitance  $CPE_{dl}$  [30,31].  $R_{ct}$  and  $CPE_{dl}$  represent the impedance connected with the interface reactions and the solid state conduction in the barrier layer. Note that impedances of ASS and LSS were at least three orders higher than CO (Fig. 11(c)), and the  $R_{ct}$  value of LSS and ASS increased by two more orders of magnitude than the substrate, confirming the excellent anti-corrosion effect of superhydrophobic film on aluminum, as well as the great contribution of air in maximizing anti-corrosion property.



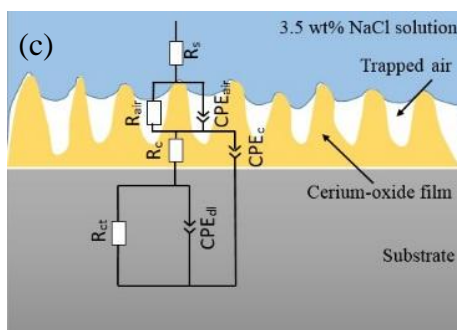


**Figure 12.** Equivalent circuits of (a) substrate. (b) coated cerium-oxide film. (c) LSS and ASS.

To analyze the impedance data accurately, the equivalent circuit models were put forward. Three different equivalent circuits were proposed to characterize the interfaces and fit the measured EIS data of substrate, CO, LSS and ASS, respectively, as shown in Fig.12. Fig.12 (a) and (b) were designed to fit all the experimental results for the substrate and CO after 40 min of immersion in the sodium chloride solution.  $CPE_c$ ,  $R_c$  and  $R_s$  correspond to the film capacitance, film resistance and solution resistance. In the case of LSS and ASS, a rough surface with a hierarchical micro-nanostructure could trap air at the solid-liquid interface, thus the equivalent circuit model had three time constants, as shown in Fig. 12(c).  $R_{air}$  and  $CPE_{air}$  were associated with the resistance and capacitance of air trapped within the hierarchical micro-nanostructure.

**Table 2.** Electrochemical model impedance parameters

samples	$R_{air}$ ( $\Omega \cdot cm^2$ )	$CPE_{air}$ ( $\Omega^{-1} s^{n_1} cm^{-2}$ )	$n_1$	$R_c$ ( $\Omega \cdot cm^2$ )	$CPE_c$ ( $\Omega^{-1} s^{n_2} cm^{-2}$ )	$n_2$	$R_{ct}$ ( $\Omega \cdot cm^2$ )	$CPE_{dl}$ ( $\Omega^{-1} s^{n_3} cm^{-2}$ )	$n_3$
substrate	--	--	--	--	--	--	7510	0.000698	0.7671
CO	--	--	--	97.59	0.0001147	0.7379	$3.096 \times 10^4$	0.0006261	0.757
LSS	$9.043 \times 10^5$	$2.044 \times 10^{-5}$	1	$1.357 \times 10^5$	$5.809 \times 10^{-9}$	0.8248	$5.322 \times 10^5$	$1.932 \times 10^{-7}$	0.8026
ASS	$2.298 \times 10^6$	$9.423 \times 10^{-6}$	1	$8.803 \times 10^5$	$1.266 \times 10^{-9}$	0.8927	$1.065 \times 10^6$	$1.91 \times 10^{-7}$	0.6892

The representative fitted parameters were summarized in Table 2.  $R_{ct}$  was found to rapidly increase when cerium-oxide film formed on aluminum.  $R_{ct}$  value of LSS and ASS increased by more than two orders of magnitude than the substrate. This emphasized the fact that cerium-oxide film and superhydrophobic film could protect the substrate effectively. The  $R_{air}$  value of LSS and ASS were  $9.043 \times 10^5 \Omega \cdot cm^2$  and  $2.298 \times 10^6 \Omega \cdot cm^2$ . The high resistance of air layer indicated that the air cushion played an important role in improving the anticorrosion of aluminum, and good agreement existed between the experimental and fitted values. Comparing the impedance parameters between LSS and ASS, it indicated that CVD method was superior to liquid-phase method.

#### 4. CONCLUSIONS

Cerium-oxide film with a micro/nano-scale hierarchical structure was fabricated on aluminum surface by a hydrothermal process. The boiling water treatment is an facile and environmentally-friendly method to pretreat the aluminum substrate, and vital to fabricate the flower-like rough structure. Superhydrophobicity of cerium-oxide film could be easily gained by a novel CVD method. As the immersion time extended, the SA decreased and the corrosion potential considerably shifted to the positive direction, showing the enhancement of corrosion resistance. This change was related to the contact state, which transferred from Wenzel state to Cassie–Baxter state. At Cassie–Baxter state, a stable air layer formed on the superhydrophobic surface, which was vital to the superhydrophobic film's anticorrosion property. FTIR results indicated that the CVD method was more efficient than liquid-phase method for superhydrophobic modification by PFOTES deposition. Furthermore, in combination with the results of LP,  $E_{oc-t}$  and EIS, ASS can be concluded to have superior corrosion resistance than LSS. The excellent anticorrosion property was attributed to the trapped air cushion in the hierarchical micro-nanostructure for the Cassie–Baxter state of superhydrophobic surface.

#### ACKNOWLEDGEMENTS

This authors gratefully acknowledge financial support from the National Natural Science Foundation of China (No. 50701006 and No. 51271031), the Fundamental Research Funds for the Central Universities (FRF-SD-12-027A and FRF-BR-13-034), National Basic Research Program of China (973 Program) ( No. 2014CB643300) and the National Environmental Corrosion Platform (NECP).

#### References

1. X.F. Gao, L. Jiang. *Nature*, 432 (2004) 36.
2. Z.G. Guo, W.M. Liu. *Plant Science*, 172 (2007) 1103.
3. T.L. Sun, L. Feng, X.F. Gao, L. Jiang. *Acc. Chem. Res.*, 38 (2005) 644.
4. W. Barthlott, C. Neinhuis. *Planta*, 202 (1997) 1.
5. L. Feng, S.H. Li, Y.S. Li, H.J. Li, L.J. Zhang, J. Zhai, Y.L. Song, B.Q. Liu, L. Jiang, D.B. Zhu. *Adv. Mater.*, 14 (2002) 1857.
6. X.J. Feng, L. Jiang. *Adv. Mater.*, 18 (2006) 3063.
7. M. Nosonovsky, B. Bhushan. *CURR OPIN COLLOID IN*, 14 (2009) 270.
8. H. Gau, S. Herminghaus, P. Lenz, R. Lipowsky. *Science*, 283 (1999) 46.
9. H. Zhang, R. Lamb, J. Lewis. *Sci. Technol. Adv. Mater.*, 6 (2005) 236.
10. F.Z. Zhang, L.L. Zhao, H.Y. Chen, S.L. Xu, D.G. Evans, X. Duan. *Angew. chem. Int. Ed.*, 47 (2008) 2466.
11. P. Wang, D. Zhang, R. Qiu, B.R. Hou. *Corros. Sci.*, 53 (2011) 2080.
12. P. Wang, D. Zhang, R. Qiu, J.J. Wu, Y. wan. *Corros. Sci.*, 69 (2013) 23.
13. Z.W. Wang, Q. Li, Z.X. She, F.N. Chen, L.Q. Li. *J. Mater. Chem.*, 22 (2012) 4097.
14. T. Liu, S.G. Chen, S. Cheng, J.T. Tian, X.T. Chang, Y.S. Yin. *Electrochimica Acta*, 52 (2007) 8003.
15. T. Ishizaki, J. Hieda, N. Saito, N. Saito, O. Takai. *Electrochimica Acta*, 55 (2010) 7094.
16. I. Torchinsky, M. Molotskii, G. Rosenman. *J. Nanopart Res.*, 12 (2010) 2427.
17. P. Wang, D. Zhang, R. Qiu. *Corros. Sci.*, 54 (2012) 77.
18. T. He, Y.C. Wang, Y.J. Zhang, Q. Lv, T.G. Xu, T. Liu. *Corros. Sci.*, 51 (2009) 1757.

19. R.N. Wenzel. IND ENG CHEM, 28 (1936) 988.
20. A. B. D. Cassie, S. Baxter,. *Trans. Faraday Soc.*, 40 (1944) 546.
21. S.S. Latthe, A.B. Gurav, C.S. Maruti, R.S. Vhatkar. *Journal of Surface Engineered Materials and Advanced Technology*, 2 (2012) 76.
22. W.G. Fahrenholtz, M.J. O'Keefe, H.F. Zhou, J.T. Grant. *Surface & Coatings Technology*, 155 (2002) 208.
23. A. Decroly, J.P. Petitjean. *Surface & Coatings Technology*, 194 (2005) 1.
24. J.L. Tang, Z.Z. Han, Y. Zuo, Y.M. Tang. *Appl. Surf. Sci.*, 257 (2011) 2806.
25. J. Liang, Y.C. Hu, Y.H. Fan, H. Chen. *Surf. Interface Anal*, 45 (2013) 1211.
26. T. Ishizaki, N. Saito. *Langmuir*, 26 (2010) 9749.
27. T. Ishizaki, Y. Masuda, Mi. Sakamoto. *Langmuir*, 27 (2011) 4780.
28. Y.B. Chen, H. Kim. *Appl. Surf. Sci.*, 255 (2009) 7073.
29. M.S. Islam, N. Akter, M.R. Karim. *Colloids and Surfaces A: Physicochemical and Engineering Aspects*, 362 (2010) 117.
30. A. Delimi, E. Galopin, Y. Coffinier, M. Pisarek, R. Boukherroub, B. Talhi, S. Szunerits. *Surface & Coatings Technology*, 205 (2011) 4011.
31. J. Liang, Y.C. Hu, Y.Q. Wu, H. Chen. *Surface & Coatings Technology*, 240 (2014) 145.

© 2015 The Authors. Published by ESG ([www.electrochemsci.org](http://www.electrochemsci.org)). This article is an open access article distributed under the terms and conditions of the Creative Commons Attribution license (<http://creativecommons.org/licenses/by/4.0/>).